



Microstructure and Mechanical Properties of Mg–2.0Gd–1.2Y–1.0Zn–0.2Zr Alloy

Jianan Liu¹ · Xiaoru Zhang¹ · Wenxue Lv¹ · Yumei Zhou¹ · Daqing Fang¹ · Xiangdong Ding¹ · Jun Sun¹

Received: 11 March 2020 / Accepted: 1 June 2020 / Published online: 22 June 2020
© The Korean Institute of Metals and Materials 2020

Abstract

The microstructural evolution of Mg–2.0Gd–1.2Y–1.0Zn–0.2Zr (GWZK) alloy during homogenization and subsequent aging heat-treatment and the tensile properties of the peak-aged sample at various temperatures have been investigated. The phase transformation during homogenization, static precipitation during aging, and deformation mechanisms at 250 °C are systematically analyzed through XRD, TEM and EBSD measurements. The peak-aged GWZK alloy has good combination of strength and ductility at elevated temperatures owing to its high thermal stability by the LPSO phases distributed along the grain boundaries. The change (19 MPa) in the yield strength of peak-aged samples between RT and 250 °C is mainly related to easy gliding of dislocations on the non-basal planes due to the decrease in critical resolved shear stress of slip. Two strengthening models are applied to quantitatively describe the effect of $\left\{ 11 \bar{2} 0 \right\}_{\alpha}$ precipitate plates on Orowan strengthening corresponding to RT and 250 °C. Ignoring changes in solid solution strengthening and grain boundary strengthening of the peak-aged sample caused by increasing temperature, the calculated reduction value (16.5 MPa) in macroscopic yield strength from RT (based on the basal $\langle a \rangle$ slip mode) to 250 °C (based on the pyramidal $\langle c + a \rangle$ slip mode) is in good agreement with the measured reduction value (19 MPa).

Keywords Mg alloy · Microstructure · Mechanical properties · Dislocation · Precipitate · Thermal stability

1 Introduction

Owing to the imperious demand for energy conservation and emission reduction, magnesium and its alloys, which possess competitive features such as low density, high specific strength, good damping capacity and excellent cast-ability [1], have received strong research interest for applications to various structural components of automobiles and aircrafts. It is reported that the addition of rare earth (RE) elements to magnesium can achieve high strength at room temperature. Since the solubility of the RE elements drastically decreases with decreasing temperature, these alloys show precipitation hardening by aging treatment. However, the thermal stability in terms of previously developed magnesium alloys is still

inferior due to the fact that grain growth tends to occur at elevated temperature.

Recently, the Mg–RE–Zn alloys containing long period stacking ordered (LPSO) phases have been considered as the promising materials [2–4]. Among these LPSO phases, the “bulk” interdendritic LPSO phases exhibit higher thermal stability [5], elastic modulus [6, 7], and microhardness [8, 9] compared with the α -Mg matrix. In addition, the plastic anisotropy of the block-shaped LPSO phases [10, 11], which shows similarity to texture, plays an enhanced role on strength, and deformation kinks of LPSO phase [11–13] also contribute to the ductility to some extent. In contrast, the strengthening effect of the thin-platelet LPSO phases is much less than that of the “bulk” interdendritic LPSO phases, since the building blocks of LPSO are aligned parallel to the $(0002)_{\alpha}$ basal plane and provide poor barriers for basal dislocations [14–16]. Therefore, LPSO phases with different morphologies have significantly different effects on mechanical properties. Hereafter, considerable reports [17–23] have systematically studied the effects of LPSO phases with different morphologies and distributions on the mechanical properties in the room temperature, and

✉ Daqing Fang
fangdaqing@xjtu.edu.cn

¹ State Key Laboratory for Mechanical Behavior of Materials, Xi’an Jiaotong University, Xi’an 710049, Shaanxi, People’s Republic of China

general conclusions are as follows: (i) “bulk” interdendritic LPSO phases improve both strength and ductility; (ii) intragranular thin-platelet LPSO phases hardly improve the strength; (iii) alternate distribution of lamellar-shaped LPSO phase and α -Mg matrix increases the yield strength but decreases the ductility. To sum up, the combination of the α -Mg matrix and harder “bulk” interdendritic LPSO phases may contribute to obtain good mechanical properties of Mg/LPSO alloys at both ambient and elevated temperatures. Therefore, it is expected to develop a new type of high-strength Mg–RE based alloy containing bulk LPSO phase with a proper volume fraction. Yamada et al. [24] investigated the effect of Zn addition on the mechanical properties of the Mg–2.0Gd–1.2Y–0.2Zr alloy, and found that 0.2% proof stress and tensile strength slightly decreases while elongation remarkably increases with an addition of Zn up to 1.0 at%. Honma et al. [25] reported that the Mg–2.0Gd–1.2Y–1.0Zn–0.2Zr (at%) alloy with LPSO structure has both high strength and excellent ductility at room temperature.

In the past, most studies on the mechanical properties of magnesium alloys containing LPSO phases with different morphologies focused on room temperature, but little attentions have been paid to thermal stability of them at elevated temperature. In this study, Mg–2.0Gd–1.2Y–1.0Zn–0.2Zr alloy (at%) was subjected to solution and aging treatment to obtain the combination microstructure of nanoscale precipitates and interdendritic LPSO phases. The mechanical properties and thermal stability of peak-aged GWZK alloy deformed in the range of RT to 250 °C were examined. The change in the yield strength of peak-aged Mg–2.0Gd–1.2Y–1.0Zn–0.2Zr alloy was quantified by model formula.

2 Experimental Procedures

2.1 Materials and Sample Preparation

An alloy ingot of composition Mg–2.0Gd–1.2Y–1.0Zn–0.2Zr (at%) (denoted as GWZK hereinafter) was prepared using semi-continuous cast by melting high pure Mg (≥ 99.9 wt%), Zn (≥ 99.9 wt%), Mg–20RE (RE = Gd, Y, wt%) and Mg–30Zr (wt%) master alloys in an electric-resistant furnace under the protection of mixture of CO₂ and SF₆ with the volume ratio of 99:1. During the semi-continuous casting process, the ingot was pulled down with a speed of 25 mm/min and the water pressure working on the crystallizer was ~ 0.02 MPa. The size of the obtained cast ingot was $\Phi 250$ mm \times 600 mm (diameter \times length). Samples segmented from the ingot were immersed into MgO powder and solution treated at 500 °C for 12 h, followed by quenching into warm water

at ~ 70 °C (denoted as T4 hereinafter), and then aged at 200 °C for different holding time ranging from 0 to 450 h. Hardness values were obtained using a Vickers hardness tester with a load of 5 kg. An average of ten measurements was used to evaluate the hardness values and ensure the accuracy and reliability of the acquired data.

2.2 Mechanical Testing

The mechanical properties of the GWZK alloy were evaluated by performing tensile tests on cylindrical samples with diameter 5 mm and gauge length 25 mm referenced to standard GB/T 228.2–2015. The tensile tests were performed using an Instron-type tester equipped with a heating chamber at a constant strain rate of 5×10^{-4} s⁻¹.

2.3 Microstructure and Deformation Mechanism Analyses

The microstructure of the samples was observed by an optical microscope (Zeiss, Neophot-32), a scanning electron microscope (Zeiss, Gemini500) equipped with an X-ray energy-dispersive spectrometer (EDS) and a transmission electron microscope (JEOL, JEM-2100Plus). The constituent phases in the alloy were examined by X-ray diffractometer (XRD: X'Pert PRO with Cu K α radiation) operated at 40 kV and 40 mA, a relatively low scanning speed (4°/min) was selected to scan from 20° to 90° in order to clearly distinguish tiny peaks via increased signal/noise ratio. The volume fraction of secondary phase was measured by Image-J software based on gray contrast, and the grain size in the alloys was measured by the liner intercept method in OM observation. As-cast and solution-treated samples were polished mechanically and then etched for 4–10 s in 4% nitric acid and in a solution of 5 g picric acid, 5 ml acetic acid, 10 ml water, 100 ml ethyl alcohol for microstructure observation, respectively. All samples for transmission electron microscopy (TEM) were cut into 0.8 mm thick slices using an electric-discharge machine. Discs 3 mm in diameter were punched from these slices, ground to a thickness of 80–100 μ m, and then twin-jet electro-polished in a solution of 5.3 g lithium chloride, 11.2 g magnesium perchlorate, 500 ml methanol and 100 ml 2-butoxyethanol at ~ 50 °C and 20–30 mA. Lastly, low energy beam ion thinning was carried out in order to eliminate the fine oxide film formed on the surface during electrolytic polishing. Microstructural data were collected using EBSD, which was performed in beam-control mode using SU3500 scanning electron microscope equipped with an Oxford Instruments-HKL Channel 5 EBSD system. Representative regions were mapped using a step size of 0.25 μ m.

3 Results and Discussion

3.1 Microstructure and Composition in the As-cast and Solution-treated Conditions

Figure 1a, b show the SEM-BSE micrograph and EDS mapping of the as-cast GWZK alloy, respectively. The microstructure of as-cast alloy consists of the primary α -Mg phase and eutectics formed in the interdendritic region. By analysis of EDS in the SEM mode (Fig. 1e), the

composition of α -Mg matrix in as-cast condition is determined to be Mg–0.53Gd (at%). Figure 1b shows the concentration distribution of eutectic, which illustrates that the eutectic is composed of α -Mg phase and β phase [26] displaying a fishbone-like shape. The β phase in eutectic is rich in Gd, Y, and Zn elements. EDS in SEM mode analysis (Fig. 1e) reveals that the composition of fishbone-like β phase is Mg–18.44Gd–7.39Y–6.79Zn (at%) whose atomic ratio is close to (Mg, Zn)₃RE phase. Figure 2 shows the XRD pattern of the GWZK alloy. Only two phases designated as α -Mg and (Mg, Zn)₃RE can be recognized from

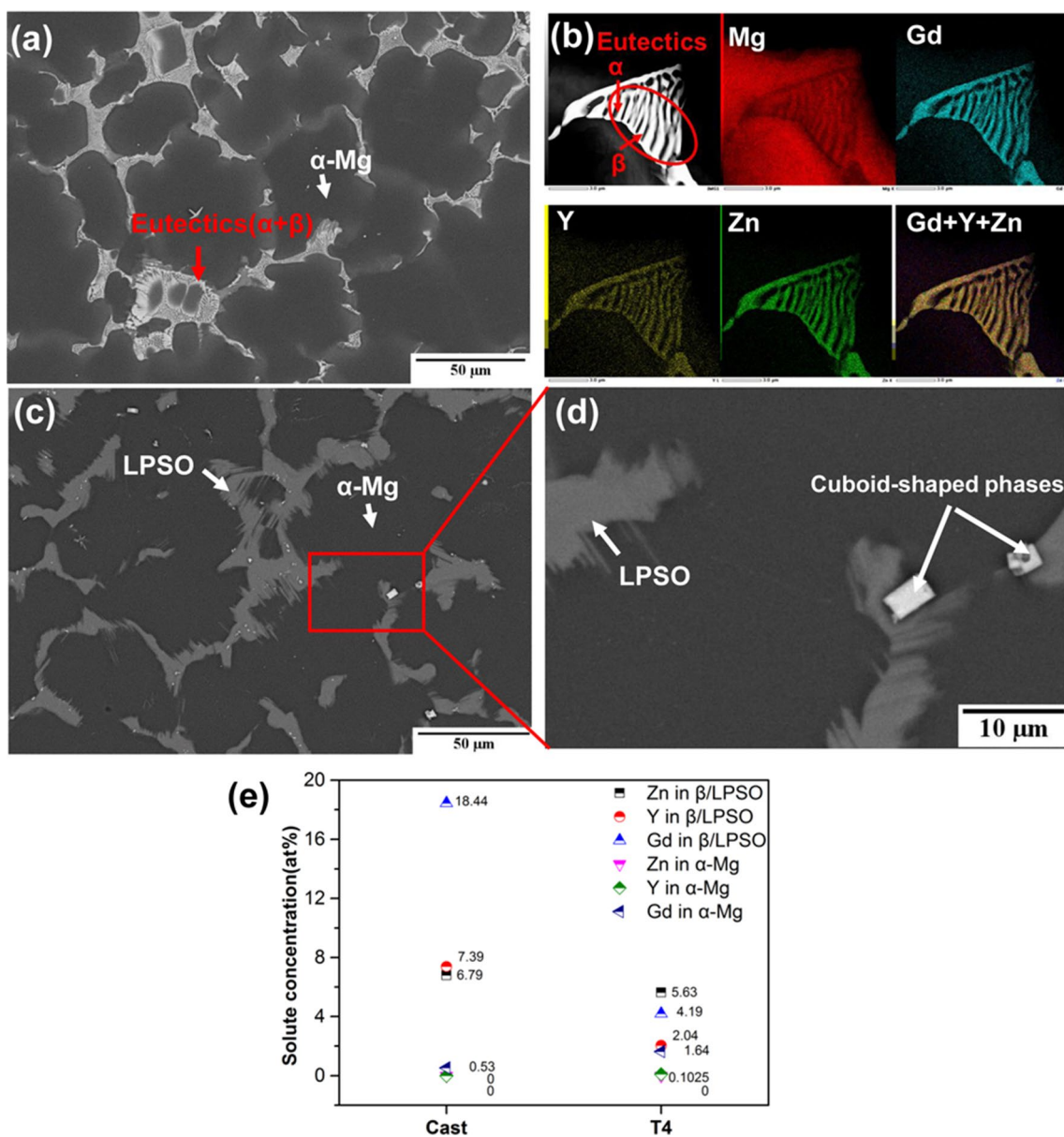


Fig. 1 a SEM-BSE image and b EDS mapping of the as-cast GWZK alloy; c optical micrograph SEM-BSE image of the solution-treated GWZK alloy; d enlarged SEM-BSE image of red rectangular region

in c; e EDS analysis on solute concentration in the interdendritic region and α -Mg matrix before and after solution treatment

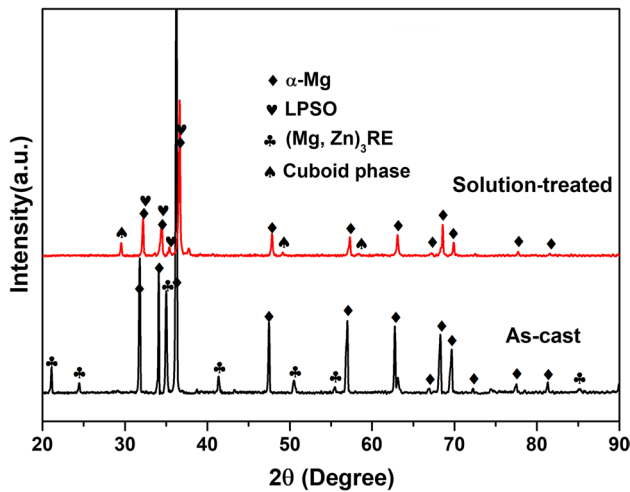


Fig. 2 XRD patterns of GWZK alloy in the as-cast and solution-treated conditions

the as-cast results. Combining the EDS with XRD results, the fishbone-like β phase may be regarded as $(\text{Mg}, \text{Zn})_3\text{RE}$. This finding is also in agreement with the investigation of Yin et al. [27]. The average grain size is 51.6 μm .

Figure 1c, d show the SEM-BSE micrographs of the solution-treated GWZK alloy. The SEM-BSE micrographs show that a solid phase transformation occurs in the interdendritic region from as-cast to solution-treated condition, i.e., $(\text{Mg}, \text{Zn})_3\text{RE}$ can be transformed into LPSO phase when both the composition and stacking orders are satisfied. The solid phase transformation can also be inferred from the disappearance of diffraction peaks of $(\text{Mg}, \text{Zn})_3\text{RE}$ and the emergence of diffraction peaks of LPSO phase [28] in the Fig. 2. Moreover, chemical analysis by EDS reveals that the composition of α -Mg matrix in solution-treated condition is $\text{Mg}-1.64\text{Gd}-0.1\text{Y}$ (at%) whose Gd atomic concentration is greater than that of as-cast matrix. It can be speculated that the increase of Gd atomic concentration is derived from the diffusion of solute atoms of β phase. Therefore, it can be concluded that a part of the β phase is dissolved into the α -Mg matrix to form supersaturated solid solution, and the remaining part is transformed into the interdendritic LPSO phase. The volume fraction (V_f) of interdendritic LPSO phase is approximately 20.9%. In addition, profuse of cuboid-shaped phases embedded within interdendritic LPSO phases (marked by white arrowheads) can also be observed from Fig. 2d. The average grain size of solution-treated sample is 52.3 μm .

3.2 Age-Hardening Behavior and Precipitation in T6 Sample

The aging behavior of the GWZK alloy at 200 °C was investigated by a hardness measurement. And the

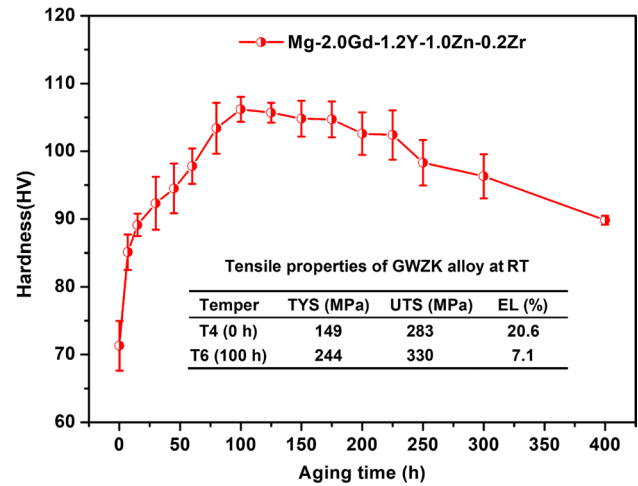
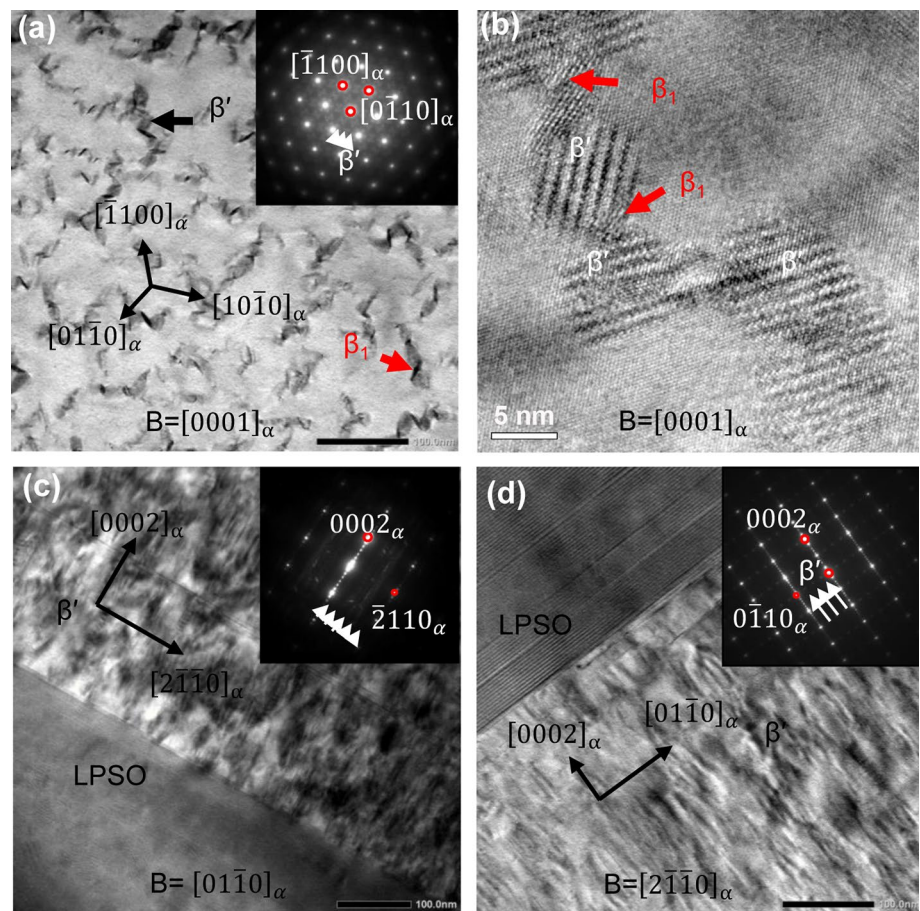


Fig. 3 Age-hardening curve of the GWZK alloy at 200 °C

age-hardening curve for the GWZK alloy is shown in Fig. 3. The age-hardening curve displays a trend that with the increasing holding time, the hardness increases rapidly and then reaches the peak hardness after aging at 200 °C for 100 h (denoted as T6 hereinafter). Further aging led to a slow decrease in the hardness. The Vickers hardness of GWZK alloy in T6 condition (102.6 HV) is 31.3 HV higher than that of GWZK alloy in T4 condition (71.3 HV). Hence, 100 h is regarded as the optimal aging time. The tensile properties of GWZK alloy at room temperature are embedded in Fig. 3. Significant improvement of ultimate tensile strength (UTS) and tensile yield strength (TYS) are observed from T4 to T6 condition, by 47 and 95 MPa, respectively, but the elongation is greatly reduced from 20.6% in T4 condition to 7.1% in T6 condition. In order to correlate the aging response with the microstructures, the structures of peak-aged GWZK alloy are investigated by TEM.

Figure 4 shows the TEM bright-field micrographs and corresponding selected area electron diffraction (SAED) patterns of peak-aged GWZK alloy with the incident electron beam parallel to $[0001]_\alpha$, $[01\bar{1}0]_\alpha$ and $[2\bar{1}\bar{1}0]_\alpha$ zone axis. Being observed along $[0001]_\alpha$ zone axis, the cross-sectional shape of the precipitates (marked by black arrowhead) shown in Fig. 4a looks like bamboo leaf. In the corresponding SAED pattern, there are extra diffraction spots at $1/4[0\bar{1}10]_\alpha$, $1/2[0\bar{1}10]_\alpha$, and $3/4[0\bar{1}10]_\alpha$, which is consistent with the precipitate with the cbco structure. Accordingly, precipitates are identified to be β' phase [29, 30] by SAED patterns. The orientation relationship implied by SAED is such that $[001]_{\beta'}/[0001]_\alpha$, $(100)_{\beta'}/(2\bar{1}\bar{1}0)_\alpha$, and the unit cell parameters are $a = 2 \times a_{\text{Mg}} = 0.64 \text{ nm}$, $b = 8 \times d(10\bar{1}0)_{\text{Mg}} = 2.28 \text{ nm}$, $c = c_{\text{Mg}} = 0.52 \text{ nm}$ [31]. Being viewed along $[01\bar{1}0]_\alpha$ and $[2\bar{1}\bar{1}0]_\alpha$ axis

Fig. 4 TEM bright-field/HRTEM images and corresponding SAED patterns of precipitates within the α -Mg matrix observed along **a**, **b** $[0001]_{\alpha}$, **c** $[01\bar{1}0]_{\alpha}$ and **d** $[2\bar{1}\bar{1}0]_{\alpha}$, respectively



zone, the precipitates show black strain contrast whose long axes point to $[0002]_{\alpha}$. From the observations on the $[0001]_{\alpha}$ and $[2\bar{1}\bar{1}0]_{\alpha}$ zone axes, the three-dimensional morphology and distribution of β' phase resembles a convex lens formed on $\{11\bar{2}0\}_{\alpha}$ prismatic plane in a dense triangular arrangement, and lateral spreading along $\langle 01\bar{1}0 \rangle_{\alpha}$ directions in $[0001]_{\alpha}$ projection and vertical spreading along $\langle 0001 \rangle_{\alpha}$ in $[01\bar{1}0]_{\alpha}$ projection. In addition, rhomb-shaped precipitate marked by red arrowhead in Fig. 4a is also confirmed in the necking of the β' phase. Local enlarged HRTEM image is shown in Fig. 4b. This phase is denoted as β_1 phase following Honma's work [25]. The formation of the β_1 phase may be attributed to strain relaxation around the β' phase. Hence, it is concluded that the high hardness is mainly achieved through simultaneous precipitation of the β' and β_1 phases during aging treatment. The structural parameters of the combination of β' and β_1 phases measured from multiple TEM bright-field images are 45.2 nm in diameter (D) and 6.3 nm in thickness (T). The volume fraction of precipitates (f_p) is calculated [32] to be 0.97%. The average grain size of peak-aged sample is 52.6 μm . It can be found that the change in grain size is negligible during the entire heat treatment process,

which suggests that the interdendritic LPSO phase can provide a strong pinning effect on grain growth at elevated temperature to keep grain boundary strengthening fixed.

3.3 Thermal Stability in Terms of Mechanical Properties for Peak-aged Samples

Figure 5 shows the stress–strain curves and mechanical properties of peak-aged samples subjected to tensile loading in the range of RT to 250 $^{\circ}\text{C}$. At RT, the ultimate tensile strength, tensile yield strength and elongation of the peak-aged sample are 330 MPa, 244 MPa and 7.1%, respectively. When enhancing the temperature from RT to 250 $^{\circ}\text{C}$, the ultimate tensile strength and tensile yield strength of the peak-aged samples decline gradually. Contrarily, the elongation improves remarkably, particularly at 250 $^{\circ}\text{C}$. The peak-aged sample still shows a good combination of strength and elongation at 250 $^{\circ}\text{C}$, its ultimate tensile strength, tensile yield strength and elongation are 293 MPa, 225 MPa and 16.8%, respectively. Even enhancing the test temperature to 250 $^{\circ}\text{C}$, the reduction in tensile yield strength is also low as 19 MPa, which indicates that the peak-aged GWZK alloy possesses extremely high thermal stability in terms of mechanical properties.

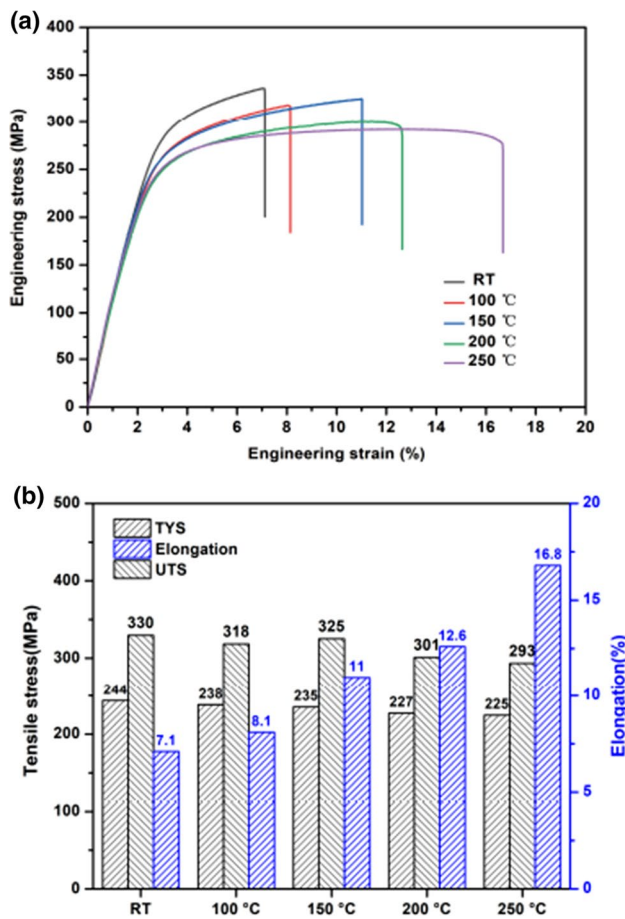


Fig. 5 a Stress–strain curves and b mechanical properties of peak-aged sample subjected to tensile loading in the range of RT to 250 °C

3.4 Deformation Mechanism in α -Mg Matrix

Figure 6a shows bright-field micrograph of the dislocation structure in peak-aged sample after uniaxial tension at 250 °C to 3%-strain observed along $[2\bar{1}\bar{1}0]_{\alpha}$ zone axis. The main feature is that there are two sets of dislocation pile-up groups (marked by white arrowheads) at the interface between the interdendritic LPSO phase and α -Mg matrix. Figure 6b shows two-beam dark-field micrograph of a local enlargement in Fig. 6a viewed $[2\bar{1}\bar{1}0]_{\alpha}$ zone axis using $\mathbf{g} = 0002_{\alpha}$ diffracting vector. From the visibility criterion analysis, the two sets of dislocations are determined to be $\langle c+a \rangle$ dislocation. The interface between the interdendritic LPSO phase and α -Mg grain can effectively pinning dislocation since there are structural and chemical differences between the LPSO phase and α -Mg solid solution [12]. Figure 6c and d show two-beam bright-field and dark-field micrographs of the dislocation structure in peak-aged GWZK alloy after uniaxial tension at 250 °C to 16.8%-strain viewed using $\mathbf{g} = 0002_{\alpha}$ diffracting vector along $[2\bar{1}\bar{1}0]_{\alpha}$ zone axis, the field of vision is the interior

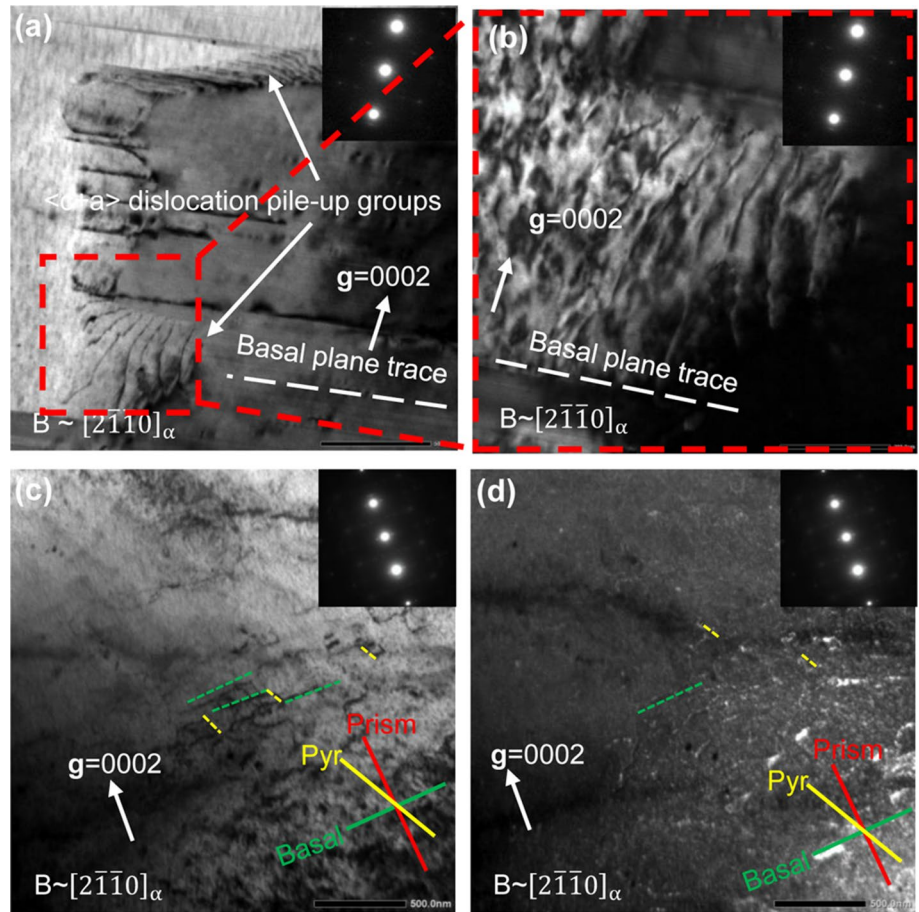
of α -Mg matrix. In Fig. 6c to Fig. 6d, dislocations visible under $\mathbf{g} = 0002_{\alpha}$ diffraction vector are $\langle c+a \rangle$ dislocations based on two-beam $\mathbf{g} \cdot \mathbf{b} = 0$ visibility analysis, the insets show the corresponding crystallographic plane traces identified using diffraction analysis, enabling determination of the crystal planes of the observed $\langle c+a \rangle$ dislocations. The dashed lines indicate that $\langle c+a \rangle$ dislocation segments are lying on basal and pyramidal planes, and $\langle c+a \rangle$ dislocations change from pyramidal plane to basal planes.

Figure 7a and b show the band contrast picture and IPF map of peak-aged sample from the longitudinal section along the tensile direction after uniaxial tension to 3%-strain at 250 °C. The deformation twinning [33–35], which is the predominant deformation mechanism to accommodate the strain along $\langle c \rangle$ direction, is hardly observed. Figure 7c shows IPF map of the longitudinal section near the tensile fracture surface of peak-aged sample after uniaxial tension to 16.8%-strain at 250 °C. The section is divided into α -Mg matrix and white region subsections. The regions with white contrasts in the IPF correspond to the interdendritic LPSO phase that cannot be identified. Color gradation representing the accumulation of dislocations is observed within individual α -Mg grain. In addition, deformation twins can also be seen in several grains. Figure 7e shows the frequency distribution of misorientation angle in 16.8%-strain sample. Rotation axis distribution corresponding to misorientation angle in the range of 80° and 90° is inserted in the Fig. 7e. According to previous results [36], it can be confirmed that the rotation axis concentrating around the $\langle \bar{1}2\bar{1}0 \rangle$ is caused by the $\{10\bar{1}2\}$ ($86^{\circ} \langle \bar{1}2\bar{1}0 \rangle$) tension twinning. Multiple $\{10\bar{1}2\}$ twin variants and their mutual intersections are observed. Consequently, $\langle c+a \rangle$ pyramidal slip is the dominant deformation mechanism in the α -Mg matrix when deformation is at 250 °C. The activation of non-basal slip systems at 250 °C facilitates the grain deformability, resulting in high elongation. And the tendency of tension twinning increases with increasing plastic deformation. The tension twinning can act a supplementary mechanism to accommodate strain along $\langle c \rangle$ direction and re-orientate the crystals to further promote the slip of dislocations. Figure 7d shows kernel average misorientation map of the same area. The green contrast characterizing the degree of plastic deformation is mostly observed at the interface between interdendritic LPSO phase and α -Mg matrix, which means that the dislocation density here is higher than that of the interior of α -Mg. This is consistent with dislocation pile-up in Fig. 6a.

3.5 Analysis of the Variation in Yield Strength

Given the distribution of interdendritic LPSO phases along grain boundaries, it can be assumed that the three-dimensional structure formed by the harder LPSO phase can be considered a strong skeleton, which can improve the ability to resist

Fig. 6 **a** Two-beam bright-field micrograph and **b** local enlarged dark-field micrograph in **a** of the dislocation structure in peak-aged sample after uniaxial tension at 250 °C to 3%-strain observed along $[2\bar{1}\bar{1}0]_{\alpha}$ zone axis, the field of vision is the interface between the interdendritic LPSO phase and α -Mg matrix; **c** two-beam bright-field micrograph and **d** dark-field micrograph of the dislocation structure in peak-aged GWZK alloy after uniaxial tension at 250 °C to 3%-strain observed along $[2\bar{1}\bar{1}0]_{\alpha}$ zone axis, the field of vision is the interior of α -Mg matrix



tensile stress. Therefore, the interdendritic LPSO phases act as a strong reinforcing component in peak-aged Mg/LPSO alloy. The yield strength of interdendritic LPSO reinforced composite is estimated by the following equations:

$$\sigma_y = \bar{\sigma}_{LPSO} V_f + \sigma'_M (1 - V_f) \tag{1}$$

$$\sigma'_M = \sigma_{SS} + \sigma_{GB} + \sigma_{Orowan} \tag{2}$$

Here σ_y is macroscopic yield strength of this composite-like Mg/LPSO alloy, $\bar{\sigma}_{LPSO}$ is an equivalent stress that the reinforcing phase bears upon yielding in the composite, $V_f (= 20.9\%)$ is the volume fraction of the interdendritic LPSO phase, σ'_M is a gross stress including σ_{SS} (solid solution strengthening), σ_{GB} (grain boundary strengthening) and σ_{Orowan} (Orowan strengthening). The Orowan equation gives the strength contribution produced by the need for dislocations to by-pass obstacles:

$$\sigma_{Orowan} = M \cdot \Delta\tau = \frac{M G b}{2\pi \lambda_p \sqrt{1 - \nu}} \ln \frac{d_p}{r_0} \tag{3}$$

where M is the average Taylor factor; $\Delta\tau$ is the increment in the critical resolved shear stress (CRSS) due to dispersion

strengthening; $G (= 17.2 \text{ GPa})$ the shear modulus of the matrix; b the magnitude of the Burgers vector of the slip dislocations; λ_p is the effective inter-particle; $\nu (= 0.35)$ the Poisson's ratio; r_0 is the dislocation core radius. In this work, precipitates in the peak-aged GWZK alloy are formed on $\{11\bar{2}0\}_{\alpha}$ prismatic plane, so it can prevent both $\langle a \rangle$ dislocation gliding on basal plane at RT and $\langle c + a \rangle$ dislocation gliding on non-basal plane at 250 °C. Nie et al. [15] and Wang et al. [36] build strengthening model:

$$\Delta\tau = \frac{G b}{2\pi \sqrt{1 - \nu} \left(0.825 \sqrt{\frac{DT}{f_p}} - 0.393D - 0.886T \right)} \cdot \ln \frac{0.886 \sqrt{DT}}{r_0} \tag{4}$$

and

$$\Delta\tau = \frac{G b}{2\pi \sqrt{1 - \nu} \left(0.935 \sqrt{\frac{DT}{f_p}} - 0.386D - 1.991T \right)} \cdot \ln \frac{1.038 \sqrt{DT}}{r_0} \tag{5}$$

to predict the increment in the CRSS of $\langle a \rangle$ dislocation gliding on basal plane $\{0001\}$ (corresponding to the deformation mechanism at RT) [36] and $\langle c + a \rangle$ dislocation

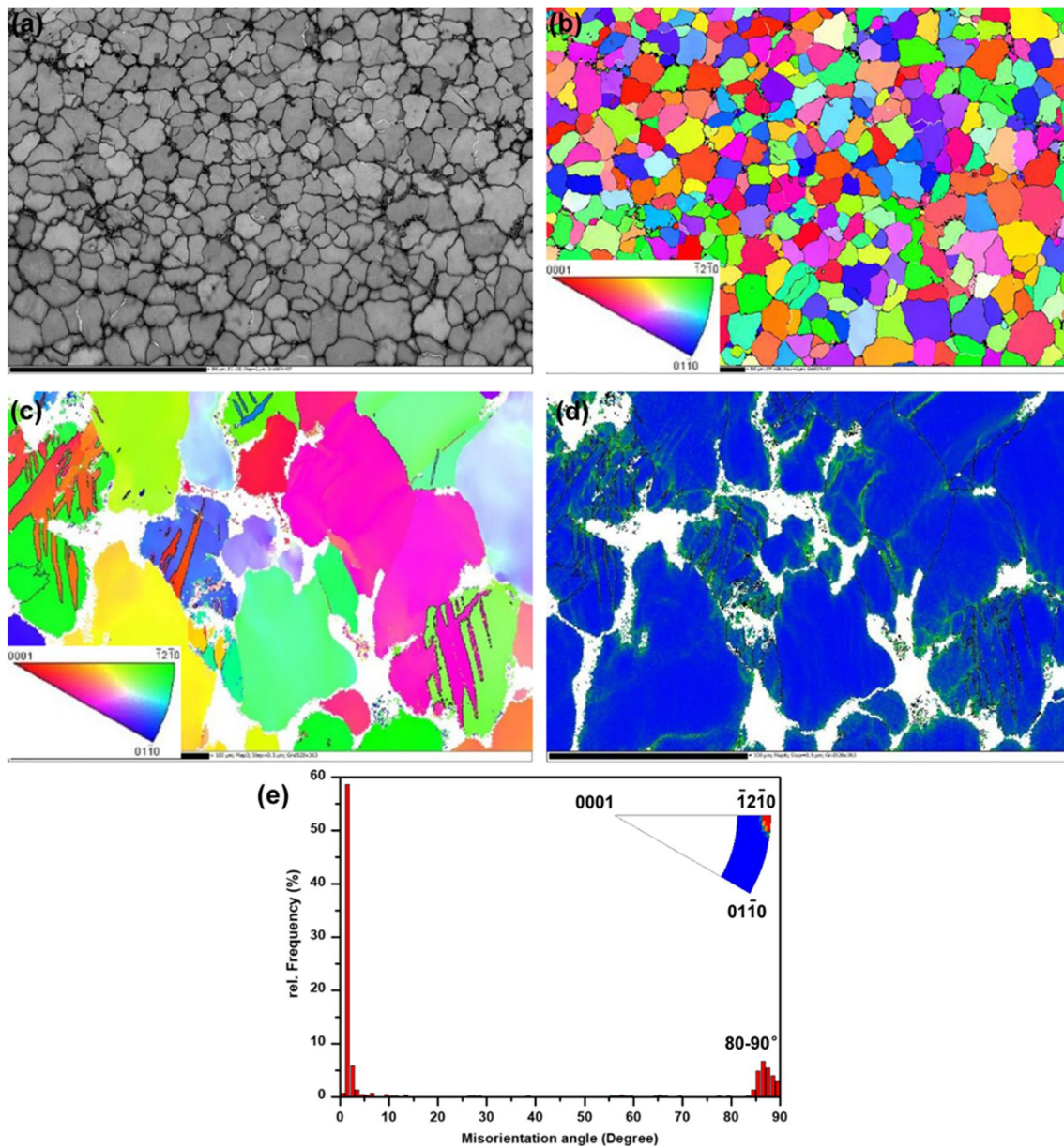


Fig. 7 **a** EBSD-Kikuchi band contrast and **b** IPF maps of the longitudinal sections of peak-aged sample after uniaxial tension to 3%-strain at 250 °C; **c** IPF and **d** kernel average misorientation maps of the longitudinal sections near the fracture surface of peak-aged sample after

uniaxial tension to 16.8%-strain at 250 °C; **e** misorientation angle distribution in **c**; The insert in **e** indicate the distribution of misorientation rotation axis for 80–90°

gliding on pyramidal plane $\{11\bar{2}2\}$, respectively. Kim et al. [37] reported that the basal $\langle a \rangle$ slip is dominant deformation mechanism in α -Mg matrix with random orientation at RT, hence, b the magnitude of the Burgers vector of $\langle a \rangle$ dislocation is 0.32 nm, and r_0 is equal to the value of b [38]. Taylor factor M is ~ 4.5 [39, 40] with a dominant $\langle a \rangle$ slip. For activated $\langle c+a \rangle$ slip at 250 °C, b the magnitude of the Burgers vector of the $\langle c+a \rangle$ dislocation is 0.61 nm and r_0 is 0.83 nm [41], Taylor factor M with a

dominant $\langle c+a \rangle$ slip is ~ 2.85 . Owing to the short test time, the change in diameter D , thickness T and volume fraction f_p of β' phase can be negligible. Substitute the structural parameters of the peak aging GWZK alloy (summarized in Table 1) into Eqs. (4) and (5) and then multiply by the corresponding Taylor factor M to calculate the precipitation strengthening values of basal and pyramidal slip modes, respectively. The calculated precipitation strengthening values of peak-aged samples deformed at RT and 250 °C are 159.3 and 138.5 MPa, respectively.

Table 1 Structural parameters of GWZK alloy in the peak-aged condition (D , T , and f_p represents the average diameter, thickness and volume fraction of the combination of β' and β_1 phases)

Dislocation type	D (nm)	T (nm)	f_p (%)	b (nm)	r_0 (nm)	M	σ_{Orowan} (MPa)
$\langle a \rangle$	45.2	6.3	0.97	0.32	0.32	4.5	159.3
$\langle c + a \rangle$				0.61	0.83	2.85	138.5

Assuming that the changes in σ_{SS} and σ_{GB} are zero between RT and 250 °C, the change in macroscopic yield strength with temperature change can be simplified as:

$$\Delta\sigma_y = [\bar{\sigma}_{LPSO}V_f + (\sigma_{GB} + \sigma_{SS} + \sigma_{Orowan})(1 - V_f)]_R - [\bar{\sigma}_{LPSO}V_f + (\sigma_{GB} + \sigma_{SS} + \sigma_{Orowan})(1 - V_f)]_E = [\bar{\sigma}_{LPSO}V_f]_R - [\bar{\sigma}_{LPSO}V_f]_E + 16.5\text{MPa} \quad (6)$$

where R and E represents room and elevated temperature, respectively. According to Hagihara et al. [10], the temperature dependence of the yield stress of interdendritic LPSO phase is negligible, so that not interdendritic LPSO phase but precipitates formed during peak aging influence the yield strength change with temperature change, i.e., $[\bar{\sigma}_{LPSO}V_f]_R - [\bar{\sigma}_{LPSO}V_f]_E$ is equal to zero. Accordingly, the calculated change in macroscopic yield strength between RT and 250 °C ($\Delta\sigma_y$) for peak-aged GWZK alloy is approximately equal to 16.5 MPa, which is in good agreement with the measured change (19 MPa).

3.6 Fracture Behavior of Peak-aged Sample

Figure 8a shows the fractography of peak-aged GWZK alloy

tested at 250 °C. The peak-aged sample exhibits the ductile fracture features of dimples and tear ridges together with the brittle fracture features of some cleavage planes and steps, as shown in Fig. 8a, which is in accordance with its high elongation of 16.8%. Consequently, the fracture mechanism of peak-aged GWZK alloy tested at 250 °C should be a mixture of ductile and brittle fracture. In addition, some large dimples containing cracked particles shown in Fig. 8b are also observed. The EDS analyses on the cracked particles confirm that they are cuboid-shaped phases containing RE element. The cracked cuboid-shaped phases surrounded by large and deep dimples suggests that they are actively involved in damage initiation and fracture process.

Fig. 8 a, b Typical fracture surfaces and c, d corresponding longitudinal cross sections near the fracture surface of peak-aged GWZK alloy tested at 250 °C

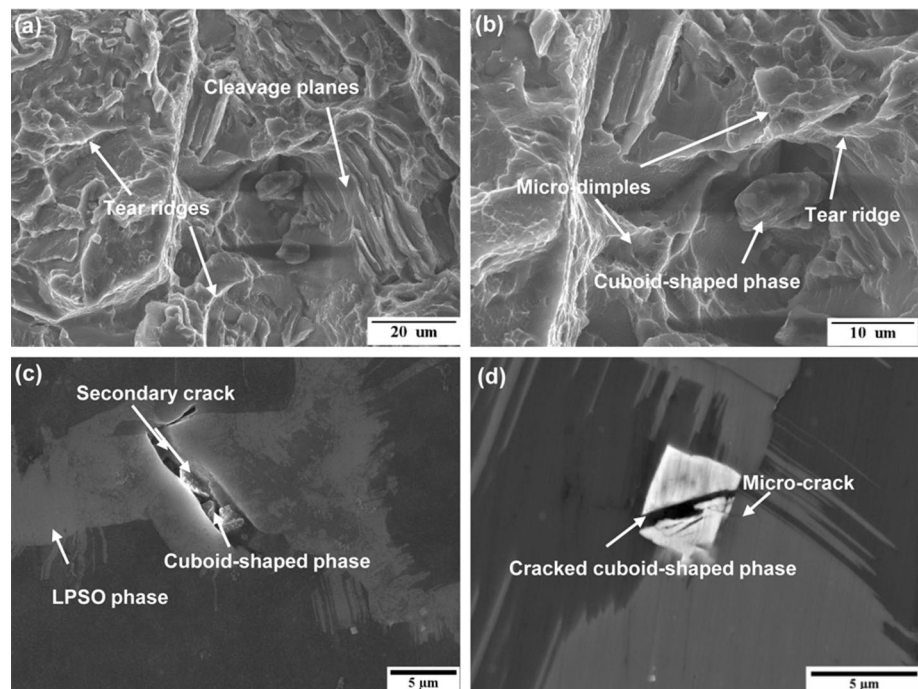


Figure 8c and d show the longitudinal cross sections near the tensile fracture surface of peak-aged GWZK alloy tested at 250 °C. It can be seen that the secondary crack occurs within the interdendritic LPSO phase (Fig. 8c). Meanwhile, several cracked cuboid-shaped phases are observed in the interior of secondary crack. Figure 8d shows that a microcrack initiates in the cuboid-shaped phase, and the crack tip has propagated into the interdendritic LPSO phase. Therefore, it can be concluded that the brittle cuboid-shaped phase is the main cracking source during deformation at 250 °C.

4 Conclusions

In this study, we comprehensively analyze the microstructure evolution, mechanical properties, deformation mechanism, thermal stability and fracture behavior of peak-aged GWZK alloy. The results can be summarized as follows:

1. After solution treatment, part of (Mg, Zn)₃RE phases is dissolved into the matrix to form supersaturated solid solution, and the remaining part of them is transformed into interdendritic LPSO phase with a volume fraction of 20.9% and cuboid-shaped phases. The high hardness of the peak-aged sample is mainly attributed to the concurrent precipitation of β' and β_1 phases formed on the $\left\{ 11 \bar{2} 0 \right\}_\alpha$ prismatic plane during aging treatment.
2. The peak-aged sample exhibits a tensile yield strength of 244 MPa and elongation of 7.1% at RT, while a tensile yield strength of 225 MPa and elongation of 16.8% at 250 °C. The yield strength loss caused by increasing temperature is only 19 MPa. The excellent thermal stability in terms of mechanical properties is related to interdendritic LPSO phase (restricting grain growth and acting as a stable reinforcement phase), intragranular β' and β_1 phases.
3. For peak-aged sample tensile tested at 250 °C, the deformation mechanism of α -Mg matrix is $\langle c+a \rangle$ pyramidal slip during initial plastic deformation. In the subsequent plastic deformation, tension twinning acting another deformation mechanism gradually appears and re-orient the crystals.
4. The precipitation strengthening value of peak-aged samples tested at RT and 250 °C is calculated to be 159.3 (based on the basal $\langle a \rangle$ slip mode) and 138.5 MPa (based on the pyramidal $\langle c+a \rangle$ slip mode), respectively. The calculated reduction value in macroscopic yield strength (16.5 MPa) is in good agreement with the measured reduction value (19 MPa).

Acknowledgements The authors gratefully acknowledge the support of Nation Natural Science Foundation of China (Grant Nos. 51931004 and 51621063) and the 111 Project 2.0 (BP2018008).

References

1. B.L. Mordike, T. Ebert, *Mater. Sci. Eng. A* **302**, 37 (2001)
2. Y. Kawamura, K. Hayashi, A. Inoue, T. Masumoto, *Mater. Trans.* **42**, 1172 (2001)
3. Y. Kawamura, M. Yamasaki, *Mater. Trans.* **48**, 2986 (2007)
4. M. Yamasaki, K. Hashimoto, K. Hagihara, Y. Kawamura, *Acta Mater.* **59**, 3646 (2011)
5. H. Okuda, T. Horiuchi, M. Yamasaki, Y. Kawamura, S. Kohara, *Scr. Mater.* **75**, 66 (2014)
6. M. Tane, Y. Nagai, H. Kimizuka, K. Hagihara, Y. Kawamura, *Acta Mater.* **61**, 6338 (2013)
7. G. Garces, D.G. Morris, M.A. Munoz-Morris, P. Perez, D. Tolnai, C. Mendis, A. Stark, H.K. Lim, S. Kim, N. Shell, P. Adeva, *Acta Mater.* **94**, 78 (2015)
8. T. Itoi, T. Seimiya, Y. Kawamura, M. Hirohashi, *Scr. Mater.* **51**, 107 (2004)
9. Y. Chino, M. Mabuchi, S. Hagiwara, H. Iwasaki, A. Yamamoto, H. Tsubakino, *Scr. Mater.* **51**, 711 (2004)
10. K. Hagihara, N. Yokotani, Y. Umakoshi, *Intermetallics* **18**, 267 (2010)
11. K. Hagihara, Y. Sugino, Y. Fukusumi, Y. Umakoshi, T. Nakano, *Mater. Trans.* **52**, 1096 (2011)
12. X.H. Shao, Z.Q. Yang, X.L. Ma, *Acta Mater.* **58**, 4760 (2010)
13. X.H. Shao, Z.Z. Peng, Q.Q. Jin, X.L. Ma, *Acta Mater.* **118**, 177 (2016)
14. Y.X. Li, D. Qiu, Y.H. Rong, M.X. Zhang, *Intermetallics* **40**, 45 (2013)
15. J.F. Nie, *Scr. Mater.* **48**, 1009 (2003)
16. C. Xu, T. Nakata, X. Qiao, M. Zheng, K. Wu, S. Kamado, *Sci. Rep.* **7**, 1 (2017)
17. C. Xu, M.Y. Zheng, K. Wu, E.D. Wang, G.H. Fan, S.W. Xu, S. Kamado, X.D. Liu, G.J. Wang, X.Y. Lv, *Mater. Sci. Eng. A* **559**, 364 (2013)
18. R. Lu, J. Wang, Y. Chen, D. Qin, W. Yang, Z. Wu, *J. Alloys Compd.* **639**, 541 (2015)
19. Y.X. Li, G.Z. Zhu, D. Qiu, D.D. Yin, Y.H. Rong, M.X. Zhang, *Alloys Compd.* **660**, 252 (2016)
20. M. Li, X. Wang, Q.Y. Feng, J. Wang, Z. Xu, P.H. Zhang, *Mater. Charact.* **125**, 123 (2017)
21. X.J. Zhou, C.M. Liu, Y.H. Gao, S.N. Jiang, X.Z. Han, Z.Y. Chen, *Metall. Mater. Trans. A* **48**, 3060 (2017)
22. X. Wu, F. Pan, R. Cheng, S. Luo, *Mater. Sci. Eng. A* **726**, 64 (2018)
23. X. Zhou, C. Liu, Y. Gao, S. Jiang, Z. Chen, *J. Mater. Eng. Perform.* **27**, 6237 (2018)
24. K. Yamada, Y. Okubo, M. Shiono, H. Watanabe, S. Kamado, Y. Kojima, *Mater. Trans.* **47**, 1066 (2006)
25. T. Honma, T. Ohkubo, S. Kamado, K. Hono, *Acta Mater.* **55**, 4137 (2007)
26. X. Zhao, J. Liu, S. Shang, X. Wang, Y. Yuan, Z. Li, Z. Han, *Mater. Charact.* **158**, 1 (2019)
27. S.Q. Yin, Z.Q. Zhang, X. Liu, Q.C. Le, Q.L. Lan, L. Bao, J.Z. Cui, *Mater. Sci. Eng. A* **695**, 135 (2017)
28. E. Onorbe, G. Garces, P. Perez, P. Adeva, *J. Mater. Sci.* **47**, 1085 (2012)
29. M. Nishijima, K. Hiraga, M. Yamasaki, Y. Kawamura, *Mater. Trans.* **47**, 2109 (2006)
30. T. Honma, T. Ohkubo, K. Hono, S. Kamado, *Mater. Sci. Eng. A* **395**, 301 (2005)

31. W.F. Xu, Y. Zhang, L.M. Peng, W.J. Ding, J.F. Nie, *Mater. Lett.* **137**, 417 (2014)
32. K. Matsumoto, S. Komatsu, M. Ikeda, B. Verlinden, P. Ratchev, *Mater. Trans. JIM* **41**, 1275 (2000)
33. Z.J. Yu, C. Xu, J. Meng, X.H. Zhang, S. Kamdo, *Mater. Sci. Eng. A* **713**, 234 (2018)
34. J.L. Li, D. Wu, R.S. Chen, E.H. Han, *Acta Mater.* **159**, 31 (2018)
35. S.Q. Zhu, S.P. Ringer, *Acta Mater.* **144**, 365 (2018)
36. F. Wang, J.J. Bhattacharyya, S.R. Agnew, *Mater. Sci. Eng. A* **666**, 114 (2016)
37. J.K. Kim, S. Sandloebes, D. Raabe, *Acta Mater.* **82**, 414 (2015)
38. Y. Wang, H. Choo, *Acta Mater.* **81**, 83 (2014)
39. C.H. Caceres, P. Lukac, *Philos. Mag.* **88**, 977 (2008)
40. J.H. Shen, Y.L. Li, Q. Wei, *Mater. Sci. Eng. A* **582**, 270 (2013)
41. P. Hidalgo-Manrique, J.D. Robson, M.T. Pérez-Prado, *Acta Mater.* **124**, 456 (2017)

Publisher's Note Springer Nature remains neutral with regard to jurisdictional claims in published maps and institutional affiliations.